SCIENCE CHINA
Information Sciences

• **Supplementary File** •

Intrinsic variations of ultrathin HfO_2-based ferroelectric tunnel junctions induced by ferroelectric-dielectric phase fluctuations

Pengying CHANG[1], Mengqi FAN[2], Gang DU[2], Xiaoyan LIU[2*] & Yiyang Xie[1*]

[1]*Key Laboratory of Optoelectronics Technology, Beijing University of Technology, Beijing* 100124*, China;*
[2]*School of Integrated Circuits, Peking University, Beijing* 100871*, China*

Appendix A Importance

Hafnium oxide (HfO_2) based ferroelectrics (FE) are promising for low power applications such as Internet of things and artificial neural network, owing to their fully CMOS-compatibility and advanced thickness scalability [1–4]. The nanoscale ferroelectric tunnel junction (FTJ) by integration of FE HfO_2 on Si/SiO_2 provides a feasible route towards realizing high-density and energy-efficient nonvolatile memory [5]. Such metal-ferroelectric-insulator-semiconductor (MFIS) FTJ with FE HfO_2 thickness around 1 to 4 nm and SiO_2 thickness below 1 nm have been demonstrated [6, 7]. Compared with FeRAM [8, 9] and FeFET [10, 11], the advantages of non-destructive read-out and reduced FE thickness in FTJ enable further voltage scaling and lower energy consumption.

For future scaling of lateral dimension of the FTJ device, it is essential to provide sufficient read current while maintaining sufficiently large ON/OFF tunneling electroresistance (TER) ratio [12]. The ferroelectric film in an FTJ is required to be as thin as possible to allow readability, but a simultaneous reduction of TER ratio is induced. To overcome the tradeoff between read current and TER ratio, selection of ferroelectric film with large remnant polarization P_r is very favorable. However, P_r of FE HfO_2 decreases with reducing film thickness [13], and thereby limiting the read current and TER ratio of HfO_2 based FTJ. It is reported that the ferroelectric properties in terms of P_r, coercive field E_c, relative permittivity ϵ_r, and grain size are strongly thickness dependent [14, 15], which can be attributed to the change in the crystalline phase [16]. For example, as FE HfO_2 film thickness decreases below 10 nm, a decline of ferroelectric phase results in the reduced P_r. In fact, the ferroelectricity in HfO_2 based thin film is reported to originate from the orthorhombic phase (o-phase) [1]. This polar phase is a metastable phase formed during the transformation between the tetragonal phase (t-phase) and monoclinic phase (m-phase) [17]. Therefore, a mixture of multiple phases (m-, o- and t-phases) possibly exists in the films, depending on various external conditions such as stress, doping, thermal treatment, and film thickness [16].

Therefore, some variability issues in ultra-scaled HfO_2-based FTJ need to be considered: (1) Co-existence of multiple phases in the FE HfO_2 film will cause random FE phase and non-FE phase fluctuation [18, 19]. Here m- and t-phases are classified as non-FE or nonpolar dielectric (DE) phase; (2) Distribution of spatial orientations of HfO_2 polycrystallines as well as various grain sizes and local doping variations will introduce P_r variation among FE grains [15, 20–22]; (3) There is a notable increase in the ϵ_r value for m-, o- and t-phase HfO_2 [14, 23–26], and hence ϵ_r variation exists in real FTJ devices accompanied with phase variations. These intrinsic variability sources will cause device-to-device variations in FE HfO_2 based devices. Though some works have studied the phase variations in the FeFET [18, 19], little is known about the variation characteristics of nanoscale FTJ devices in terms of read current and TER effect. This work aims to fully judge the FTJ variations stemming from the random phase fluctuation, P_r variation and ϵ_r variation with aggressively scaled dimensions and to guide device optimization based on fundamental understanding of the electrical behaviors.

Appendix B Simulation methodology

The Figure 1(a) and (b) of our letter show the cross-section view and 3D view of the MFIS-based FTJ structure using metal/FE $HfO_2/SiO_2/Si$ stack. Based on the NLS model, ferroelectric can be regarded as an ensemble of elementary regions characterized by independent switching kinetics [27]. The FE layer is discretized into many grains, where the uniform grain size is assumed in the simulation as done in [18, 19]. Figure B1 shows the flowchart to implement FE phase and DE phase fluctuation into FTJ based on 3D simulation. The grain number N_G within the FE film is obtained to be $N_G = (W/W_G) \times (L/L_G)$, where W and L are the device width and length, W_G and L_G are the grain width and length, respectively. Each grain is randomly assigned as DE grain based on a certain probability defined as DE phase percentage. Using this approach, the impacts of FE-DE number fluctuation and spatial fluctuation as well as grain boundary are naturally included, as shown in Figure 1(d). To further introduce the P_r variation, the remaining FE grains are assigned with different P_r values following an experimentally extracted distribution, as shown in Figure 1(e). In addition, the discrepancy of ϵ_r value for m-, o- and t-phase HfO_2 are accounted by assigning FE grains with o-phase ϵ_r value, and DE grains with randomly m- and t-phase ϵ_r value, and then ϵ_r variation of each phase is introduced similarly to P_r variation, as shown in Figure 1(f).

The 3D electrostatics of FTJ devices are obtained by performing the COMSOL simulator with drift-diffusion model. Polarization charge is treated as the surface charge density at the FE HfO_2/SiO_2 interface since the charge at the FE-metal interface is assumed to be fully screened. Note that the interface quality of HfO_2/SiO_2 and SiO_2/Si interfaces is assumed to be perfect, and thus charge trapping effect [28] is not considered here. Once obtained the band profile, the transmission probability is calculated based on

* Corresponding author (email: xyliu@ime.pku.edu.cn, xieyiyang@bjut.edu.cn)

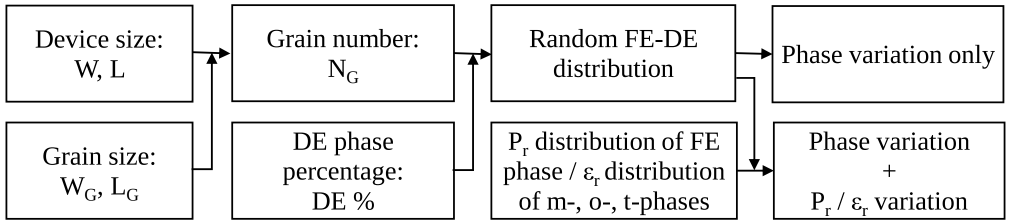

Figure B1 Simulation flowchart to implement FE and DE phase related fluctuations in FTJ based on 3D simulation.

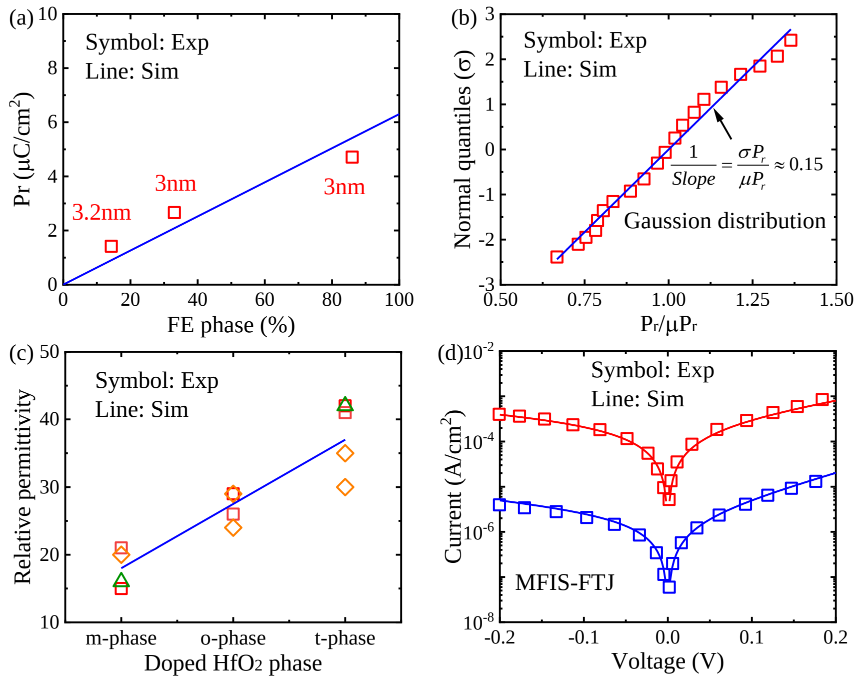

Figure B2 (a) Calibration of the P_r dependence on FE phase percentage in 3 nm thick doped HfO_2 with experimental results [16]. (b) P_r distribution of FE grains in HfO_2-based FE are assumed following Gaussian distribution based on experimental results [30]. (c) Variations of the ϵ_r of m-, o-, and t-phase doped HfO_2 are taken from [23–25]. (d) Calibration of the measured [6] and simulated I-V curves of ultrathin HfO_2-based MFIS-FTJ.

the Wentzel-Framers-Brillouin (WKB) approximation, and then the tunneling current in each grain is calculated using the Tsu-Esaki model [29, 30]. Tunneling processes including direct tunneling, FN tunneling, and thermal emission are considered, whereas the trap-assisted tunneling is ignored as the perfect dielectric quality is assumed. Due to the energy bandgap of semiconductor, tunneling current through the MFIS stack is consisted of three components: electron tunneling from the conduction band (CBE) and valence band (VBE), and hole tunneling from the valence band (VBH), and their tunneling barrier heights ϕ_{CBE}, ϕ_{VBE} and ϕ_{VBH} are related to conduction and valence band offsets respectively [29–32], as shown in Figure 1(c) of our letter. The metal electrode is assumed to be perfectly screened, while the semiconductor electrode is treated as follows. When the semiconductor surface is driven into accumulation, it can be regarded as like a metal. When the semiconductor surface is depleted of carriers by polarization reversal, tunneling through the space charge region is considered besides through HfO_2 and SiO_2 [27, 28]. The effect of FE-DE variation and resultant uniform potential on carrier transport are considered by discretizing each grain into many small regions, and then the current in this grain is obtained by taking the average value of all these regions. Then, the total current of the entire FTJ is estimated as the sum of current in each region.

To mimic the ultrathin FTJ device as realistic as possible, ferroelectric properties and physical models are calibrated with reported experimental results. Figure B2(a) shows the calibration of the P_r dependence on FE phase percentage in 3 nm thick doped HfO_2 with experimental results [16]. The P_r of mixed phase FE film linearly decreases with increasing DE phase percentage, which can be approximately expressed as (1-DE%) $\times 6\mu C/cm^2$. Due to their limited P_r and resultantly small TER ratio, impacts of FE-DE variations in such ultrathin FTJs will be more serious than thick devices, and hence this work focuses on the 3 nm HfO_2 based FTJs. Figure B2(b) shows the P_r distribution of FE HfO_2 film following Gaussian distribution based on experimental results [33]. Its normalized variation defined as the ratio of standard deviation σP_r to mean value μP_r is obtained from the slope of the normal quantile plot. Figure B2(c) shows the reported ϵ_r of HfO_2-based film [23–25], and values of 18, 25, and 35 are adopted for m-, o-, t-phase respectively. Figure B2(d) shows the I-V curves under read operation of MFIS(n+)-FTJ, indicating an excellent agreement between the measured [6] and simulated results. Here the T_{FE} and T_{IL} are 4 and 0.4 nm respectively, which are consistent with [6]. Note that variations are excluded in Figure B2(d), mainly focusing on the parameter calibrations for tunneling current calculation. The tunneling effective mass of Si is taken as 0.19 m_0, where m_0 is the vacuum electron mass, while a single effective mass approximation is adopted for the tunneling effective mass across the HfO_2 and SiO_2 and its value is calibrated to be 0.24 m_0, and more details are present in [29, 30]. For lateral dimension of FTJ, area scaling below 20 $\times$ 20 nm become possible [34],

Table B1 Default parameters used in the simulation

Symbol	Quantity	Value
T_{FE}	Thickness of HfO_2-based ferroelectric	3 nm
T_{IL}	Thickness of SiO_2 interfacial layer	4nm
ϵ_r	Relative permittivity of FE HfO_2	8 (m), 25 (o), 35 (t)
ϵ_{rIL}	Relative permittivity of SiO_2	3.9
ϵ_{rS}	Relative permittivity of Si	11.9
N_D	Donor doping concentration of Si	$5 \times 10^{19} cm^{-3}$
ϕ_M	Work function of metal electrode	4.3 eV
$DE\%$	DE phase percentage	0%, 10%, 50%
P_r	Remnant polarization of ferroelectric	(1-DE%) $\times$ 6 $\mu C/cm^2$
W	Device width = device length (L)	50, 100, 200 nm
W_G	Grain width = grain length (L_G)	5, 10, 20 nm
V_{read}	Applied voltage for read operation	0.2 V

while reported grain size of FE HfO_2 has a broad radius range (3-30 nm) [15,35]. Read voltage V_{read} of 0.2 V is low enough that polarization direction will not be switched during read operation. Simulation parameters for metal/FE-HfO_2/SiO_2/Si(n+) FTJ devices including device structure parameters are summarized in Table B1, where T_{FE} and T_{IL} are 3 and 0.4 nm, donor doping concentration of Si is $5 \times 10^{19} cm^{-3}$, and metal work function ϕ_M is 4.3 eV, respectively. Statistical samples of 100 FTJs are simulated.

Appendix C Impact of sole FE-DE phase fluctuation

For Figure 1(h) in our letter, as the DE phase percentage increases from 0%, 10% to 50%, the effective sensing margin reduces with TER ratio (taken as the ratio of J_{ON} to J_{OFF}) degrading from 14, 19, to 10, due to the P_r decrease of the entire FE film. It is noteworthy that DE phase of only 10% has generated significant variations of read current in FTJ devices. However, DE phase even above 75% has very limited effect on the memory window (MW) and current variation for the FeFET [18]. This can be explained that MW of FeFET is theoretically approximated as $2T_{FE} \times E_c$, which is irrelevant to the P_r unless it is below a very small value [36]. In contrast, the tunneling currents and TER ratio are directly determined by the P_r, and consequently FTJ device seems to be more vulnerable to mixed phase fluctuation than FeFET.

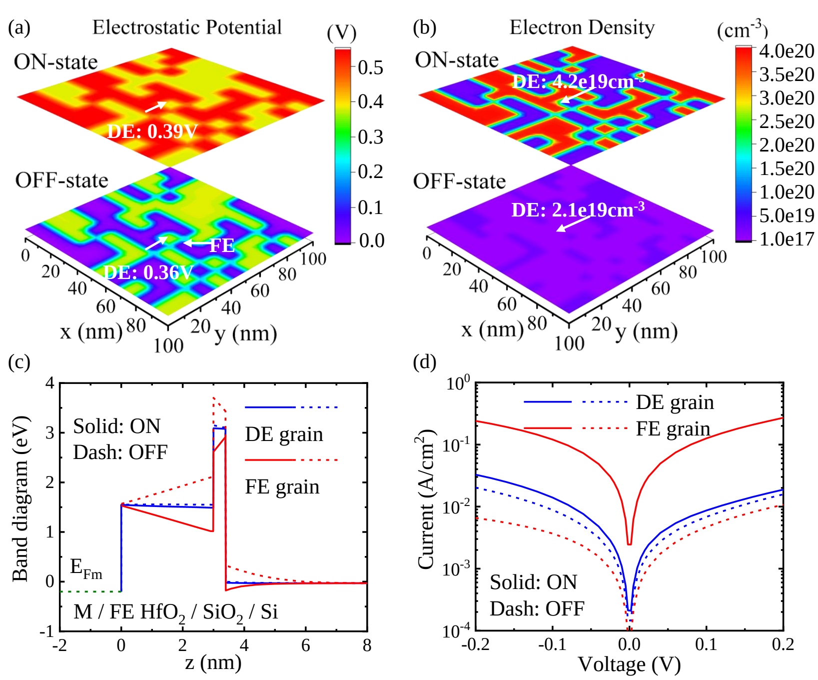

Figure C1 Profiles of (a) electrostatic potential and (b) electron density at the semiconductor surface of a certain FTJ with 50% DE phase at 0.2 V. (c) Band diagrams and (d) I-V curves of the adjacent DE and FE grain as labeled in (a). Note that the potential in (a) is shifted to 0 V.

Figure C1(a) and (b) shows the profiles of the electrostatic potential and electron density at the semiconductor surface of a certain FTJ with 50% DE phase at applied voltage of 0.2 V, solely considering FE-DE phase fluctuation. From Figure C1(a), when polarization direction is reversed, change of potential for FE grains is very large as expected, which can reach up to 0.5 V between ON- and OFF state. Moreover, the DE grains can be influenced by adjacent FE grains, as indicated by the change of potential about 0.03 V. This slight potential change gives rise to a marked change of electron density from $2.1 \times 10^{19} cm^{-3}$ to

$4.2 \times 10^{19} cm^{-3}$ at the position of DE grains, as seen in Figure C1(b). Therefore, polarization reversal of FE grains introduces a very tiny TER ratio of DE grains. It is clear that the impacts of number fluctuation and spatial fluctuation of the mixed crystalline phases are accurately captured by 3D simulation. Figure C1(c) shows the band diagrams of adjacent FE and DE grains under reversed polarizations. From Figure C1(d) (i.e., Figure 1(g)), tunneling currents through DE grains always lie between those of J_{ON} and J_{OFF} of FE grains. They can result in an averagely reduced J_{ON} and raised J_{OFF} for the entire FE film, and a larger number of DE grains causes a smaller entire TER ratio.

Appendix D Combined impacts of FE-DE phase fluctuation and P_r variation

Figure D1 shows the combined impacts of FE-DE phase fluctuation and P_r variation (without ϵ_r variation), in terms of J_{ON} and TER ratio at 0.2 V. Corresponding normalized variations σ/μ of J_{ON} and TER ratio are evaluated, where σ and μ are related standard deviation and mean value. Note that J_{OFF} variation is implicitly included in TER variation. For each DE phase percentage, P_r without variation ($\sigma P_r/\mu P_r = 0\%$) and with variation ($\sigma P_r/\mu P_r = 15\%$ and 30%) are compared respectively. The inhomogeneity of P_r distribution represented by the magnitude of $\sigma P_r/\mu P_r$, which is extracted from [30, 37]. From Figure D1(a), J_{ON} variation is seriously aggravated by increased inhomogeneity of P_r. In the 0% DE case, $\sigma J_{ON}/\mu J_{ON}$ is 0.035 and 0.073 in the $\sigma P_r/\mu P_r$ case of 15% and 30% respectively. In the 50% DE case, $\sigma J_{ON}/\mu J_{ON}$ for solely considering the FE-DE phase fluctuations is as high as 0.117, and it reaches up to 0.159 by the combined impacts of 30% $\sigma P_r/\mu P_r$ variation. The TER variation in Figure D1(b) shows a similar trend with J_{ON} variation, but there is a slight difference with respect to the σ/μ values due to the small J_{OFF} variation. In the 50% DE case, $\sigma TER/\mu TER$ is higher than $\sigma J_{ON}/\mu J_{ON}$. In particular, when $\sigma P_r/\mu P_r$ is above 15%, $6\sigma/\mu$ that is larger than 100% in terms of TER happens. Consequently, it is of great necessity to account for the FE-DE related variations in ultrathin FE HfO_2 FTJ devices, due to the existence of high DE percentage in the ultrathin FE HfO_2 films.

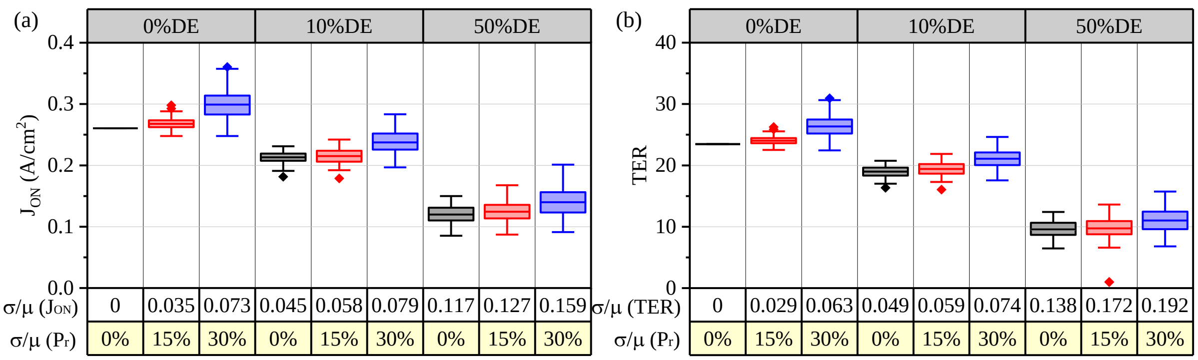

Figure D1 Combined impacts of FE-DE phase fluctuation and Pr variation. (a) J_{ON} and (b) TER ratio as a function of DE phase percentage (0%, 10% and 50%) and $\sigma P_r/\mu P_r$ (0%, 15% and 30%) respectively.

Appendix E Combined impacts of FE-DE phase fluctuation and ϵ_r variation

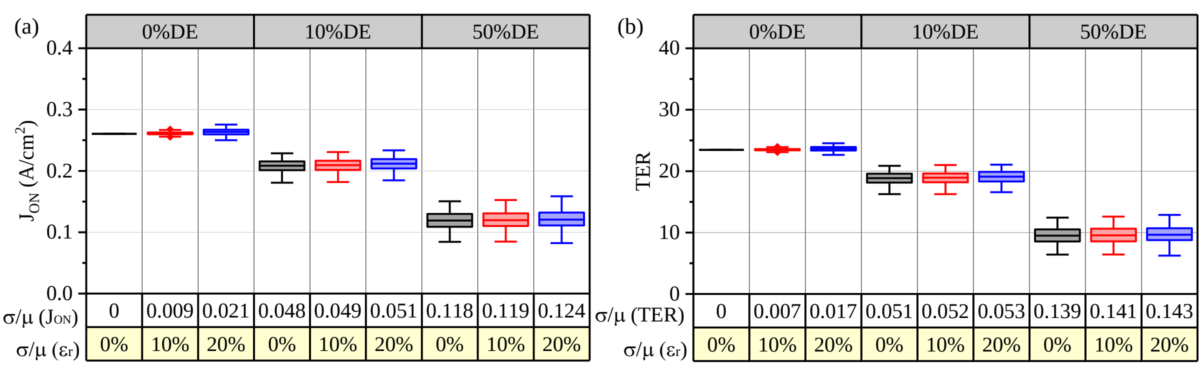

Figure E1 Combined impacts of FE-DE phase fluctuation and ϵ_r variation. (a) J_{ON} and (b) TER ratio as a function of DE phase percentage (0%, 10% and 50%) and $\sigma\epsilon_r/\mu\epsilon_r$ (0%, 10% and 20%) respectively.

Many previous works have assumed constant ϵ_r for mixed phase FE HfO_2 when analyzing the FE-DE phase fluctuation of FeFET [18, 19]. How might the ϵ_r variation affects the FE HfO_2-based devices has rarely been explored. Figure E1 shows the combined impacts of FE-DE phase fluctuation and ϵ_r variation (without P_r variation) in FE HfO_2 based FTJ. In the $\sigma\epsilon_r/\mu\epsilon_r =$ 0% case, FE grains with o-phase ϵ_r and DE grains with randomly m- and t-phase ϵ_r value are assigned in replacement of constant ϵ_r for all phases. By taking this step, changes of both $\sigma J_{ON}/\mu J_{ON}$ and $\sigma TER/\mu TER$ are only around 2%. In the $\sigma\epsilon_r/\mu\epsilon_r = 10\%$ and 20% cases, ϵ_r variations of each phase are introduced, and their impacts on FTJ variation are still quite limited. The reasons can be explained as follows. It is difficult to determine the fraction of t-phase by experimental techniques [15], and therefore DE grains are assumed with equal probability to be t- and m-phases in the simulation. Consequently, impact of lower-ϵ_r m-phase compensates that of higher-ϵ_r t-phase, and their combined impacts on FTJ performance are close to that of medium-ϵ_r o-phase. Based on the relative ϵ_r value of m-, o- and t-phase HfO_2, the average current across the DE grains consisting of lower-ϵ_r m-phase and the higher-ϵ_r t-phase HfO_2 tends to quantitatively alike the case of constant ϵ_r for all phases where the medium-ϵ_r is used. Therefore, variations of J_{ON} and TER ratio under combined impacts of FE-DE phase fluctuation and ϵ_r variation only show a very tiny increase compared with that of sole FE-DE phase fluctuation.

Appendix F Combined impacts of FE-DE phase fluctuation, P_r variation, and ϵ_r variation

To explore the worst scenario, combined impacts of the FE-DE phase fluctuation, P_r variation and ϵ_r variation are studied by assigning DE phase percentage of 50%, $\sigma P_r/\mu P_r$ of 30%, and $\sigma\epsilon_r/\mu\epsilon_r$ of 20%. Figure F1(a) shows the corresponding I-V dispersions compared with solely FE-DE phase fluctuation. Variation of read current is seriously degraded as expected. Figure F1(b) and (c) gives an instance of spatial distributions of J_{OFF} and J_{ON} at 0.2 V within a certain FTJ. To control the FE-DE phase fluctuation induced various variations, grain engineering including grain number and grain size will be investigated in the following, accounting for the abovementioned worst scenario.

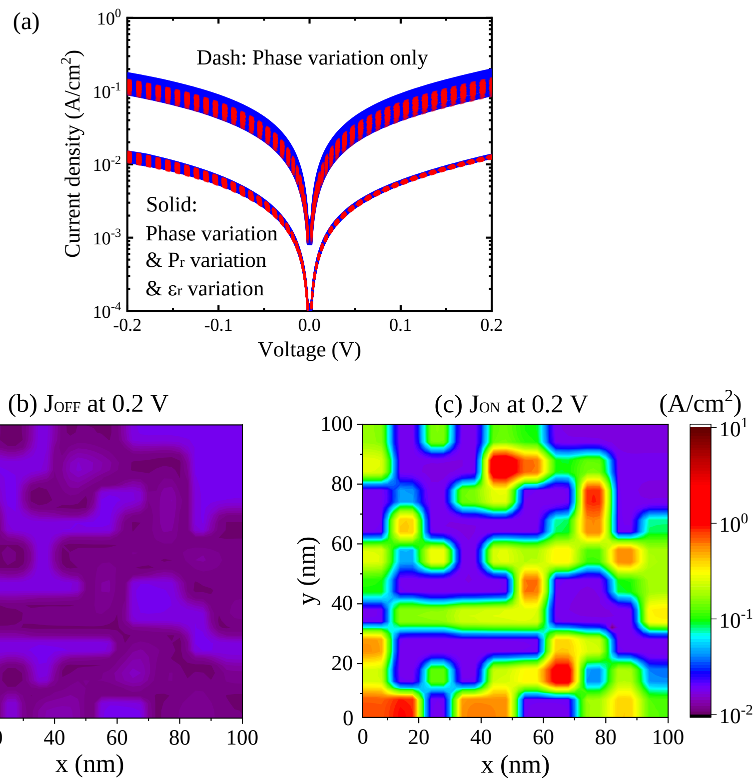

Figure F1 (a) I-V dispersions for J_{ON} and J_{OFF} during read operation of 100 FTJ devices with DE phase percentage of 50%, $\sigma P_r/\mu P_r$ of 30%, and $\sigma\epsilon_r/\mu\epsilon_r$ of 20%, considering combined impacts of FE-DE phase fluctuation, P_r variation and ϵ_r variation. Spatial distributions of (b) J_{OFF} and (c) J_{ON} of a certain FTJ at 0.2 V.

Appendix G Dependence on grain size and device size

The grain size of FE HfO_2 films has been experimentally identified to range from a few nanometers to tens of nanometers [15, 34]. Considering the combined impacts of FE-DE phase fluctuation, P_r variation and ϵ_r variation, the FTJ variations are studied by varying the relative size between the FTJ area and grain size.

First, the device size is fixed but the grain size is varied, as shown in Figure G1(a) and (b). For fixed device size of $W \times L = 100 \times 100nm$, various grain sizes of $W_G \times L_G = 20 \times 20, 10 \times 10$ and $5 \times 5nm$ are studied in terms of J_{ON} and TER respectively. As grain size decreases, device variation is significantly reduced. To be specific, $\sigma J_{ON}/\mu J_{ON}$ is reduced from 0.274, 0.166, to 0.071, and $\sigma TER/\mu TER$ is from 0.302, 0.188 to 0.079. Figure G2(a) and (b) shows the profiles of the electrostatic potential and electron density of a certain FTJ at the ON-state. Due to increased grain number, scaling of grain size reduces the randomness of number fluctuations of FE and DE grain on device level. Second, the grain size is fixed but the device size is varied as shown in Figure G1(c) and (d), where the device area scales with fixed grain size of $W_G \times L_G = 10 \times 10nm$. As lateral dimension including W and L increases from 50×50, 100×100 to 200×200 nm, device-to-device variation decreases.

Particularly, grain number of N_G are designed to be same between grain size and device size study in Figure G1, with N_G varying from 25, 100, to 400. Figure G3 shows the corresponding normalized variation σ/μ of J_{ON} and TER ratio as a function of grain number. It is found that at fixed grain number, the impact of increasing device size is analogous to that of reducing grain size, which can be verified by comparison of the $\sigma J_{ON}/\mu J_{ON}$ and $\sigma TER/\mu TER$ values. Therefore, the overall variation is directly controlled by the grain number in the FE films. For the worst scenario (namely, DE phase percentage of 50%, $\sigma P_r/\mu P_r$ of 30%, and $\sigma\epsilon_r/\mu\epsilon_r$ of 20%), grain number of 400 is required to control the FTJ variations of read current and TER ratio below 0.1.

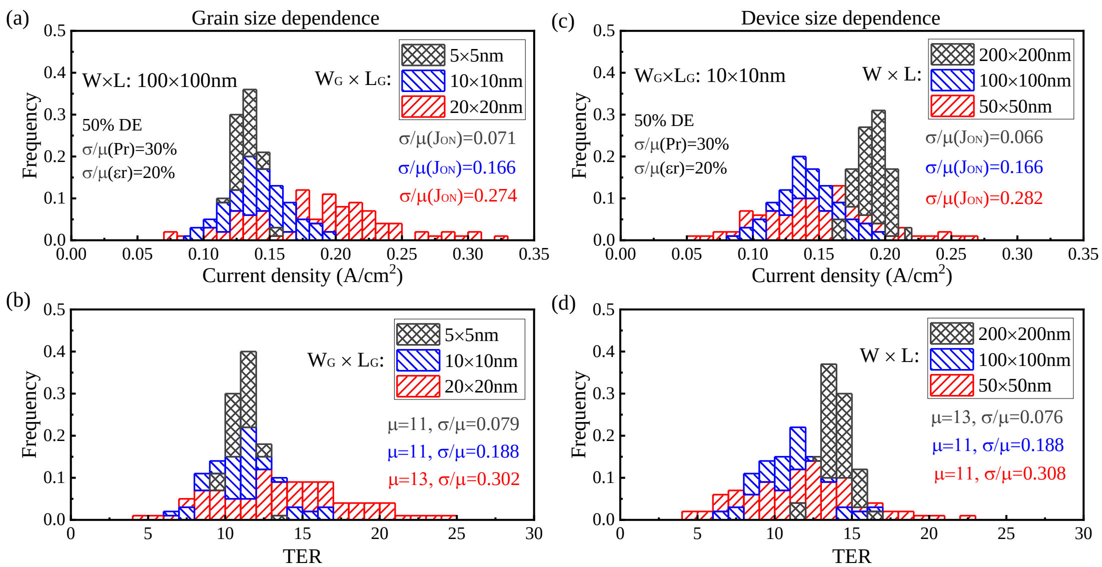

Figure G1 (a) J_{ON} and (b) TER ratio as a function grain size with fixed device size of $W \times L = 100 \times 100nm$. (c) J_{ON} and (d) TER ratio as a function device size with fixed grain size of $W_G \times L_G = 10 \times 10nm$. DE phase percentage of 50%, $\sigma P_r/\mu P_r$ of 30%, and $\sigma\epsilon_r/\mu\epsilon_r$ of 20% are considered.

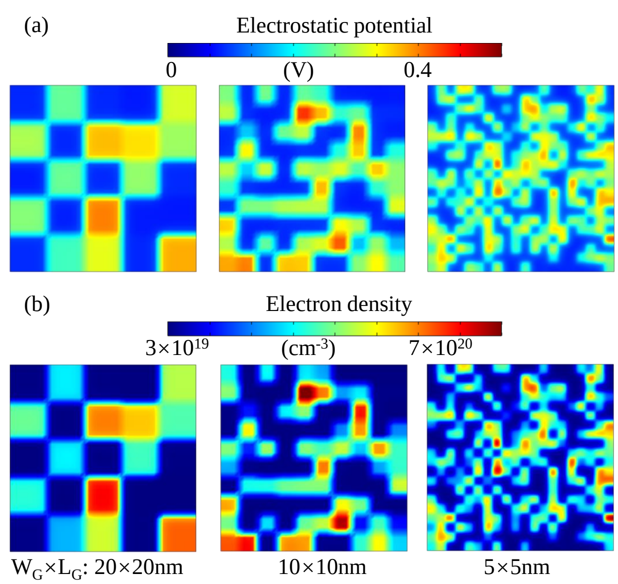

Figure G2 (a) Electrostatic potential and (b) electron density of a certain FTJ corresponding to Figure G1(a) with various $W_G \times L_G$ at the ON-state.

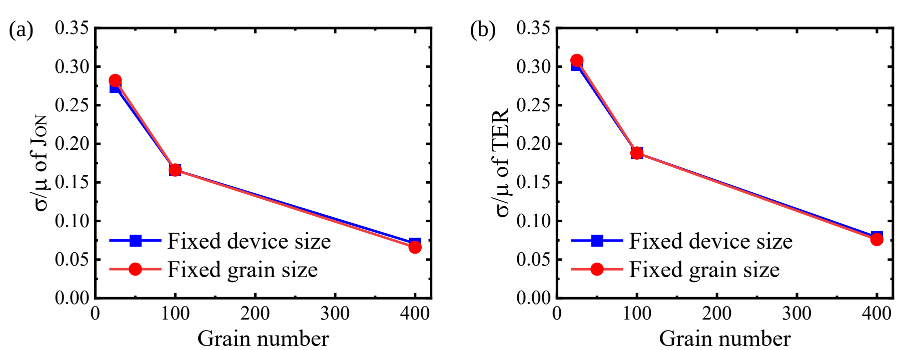

Figure G3 Normalized variation σ/μ of (a) J_{ON} and (b) TER as a function of grain number, where the values of σ/μ are extracted from Figure G1.

References

1 Boscke T S, Muller J, Brauhaus D, et al. Ferroelectricity in hafnium oxide thin films. Appl Phys Lett, 2011, 99: 102903
2 Cheng C, Tiw P J, Cai Y, et al. In-memory computing with emerging nonvolatile memory devices. Sci China Inf Sci, 2021, 64: 221402
3 Wang H, Huang Q, Yang M, et al. Deep insight into the voltage amplification effect from ferroelectric negative capacitance. Sci China Inf Sci, 2019, 62: 089401
4 Tian G, Bi J, Xu G, et al. Single-event-transient effects in silicon-on-insulator ferroelectric double-gate vertical tunneling field effect transistors. Sci China Inf Sci, 2020, 63: 229403
5 Cheema S S, Kwon D, Shanker N, et al. Enhanced ferroelectricity in ultrathin films grown directly on silicon. Nature, 2020, 580: 478-482
6 Kobayashi M, Tagawa Y, Mo F, et al. Ferroelectric HfO_2 tunnel junction memory with high TER and multi-level operation featuring metal replacement process. IEEE J Electron Devices Soc, 2019, 7: 134-139
7 Chouprik A, Chernikova A, Markeev A, et al. Electron transport across ultrathin ferroelectric $Hf_{0.5}Zr_{0.5}O_2$ films on Si. Microelectron Eng, 2017, 178: 250-253
8 Muller J, Boscke T S, Muller S, et al. Ferroelectric hafnium oxide: a CMOS-compatible and highly scalable approach to future ferroelectric memories. In: Proceedings of IEEE IEDM, Washington, USA, 2013. 280-283
9 Fan M, Chang P, Du G, et al. Impacts of radius on the characteristics of cylindrical ferroelectric capacitors. IEEE Trans Electron Devices, 2020, 67: 5810-5814
10 Dunkel S, Trentzsch M, Richiter R, et al. A FeFET based super-low-power ultra-fast embedded NVM technology for 22nm FDSOI and beyond. In: Proceedings of IEEE IEDM, San Francisco, USA, 2017. 485-488
11 Deng S, Liu Z, Li X, et al. Guidelines for ferroelectric FET reliability optimization: charge matching. IEEE Electron Device Lett, 2020. 41: 1348-1351
12 Bruno F Y, Boyn S, Fusil S, et al. Millionfold resistance change in ferroelectric tunnel junctions based on nickelate electrodes. Adv Electron Mater, 2016, 2: 1500245
13 Lyu X, Si M, Sun X, et al. Ferroelectric and anti-ferroelectric hafnium zirconium oxide: scaling limit, switching speed and record high polarization density. In: Symposium on VLSI Technology, Kyoto, Japan, 2019. 44-45
14 Muller J, Schroder U, Boscke T S, et al. Ferroelectricity in yttrium-doped hafnium oxide. J Appl Phys, 2011, 110: 114113
15 Lederer M, Kampfe T, Olivo R, et al. Local crystallographic phase detection and texture mapping in ferroelectric Zr doped HfO_2 films by transmission-EBSD. Appl Phys Letts, 2019, 115: 222902
16 Tian X, Shibayama S, Nishimura T, et al. Evolution of ferroelectric HfO_2 in ultrathin region down to 3 nm. Appl Phys Letts, 2018, 12: 102902
17 Wei Y, Nukala P, Salverda M, et al. A rhombohedral ferroelectric phase in epitaxially strained $Hf_{0.5}Zr_{0.5}O_2$ thin films. Nat Mater, 2018, 17: 1095-1100
18 Garg C, Chauhan N, Deng S, et al. Impact of random spatial fluctuation in non-uniform crystalline phases on the device variation of ferroelectric FET. IEEE Electron Device Lett, 2021, 42: 1160-1163
19 Liu Y S and Su P. Impact of trapped-charge variations on scaled ferroelectric FET nonvolatile memories. IEEE Trans Electron Devices, 2021, 68: 1639-1643
20 Chouprik A, Zakharchenko S, Spiridonov M, et al. Ferroelectricity in $Hf_{0.5}Zr_{0.5}O_2$ thin films: a microscopic study of the polarization switching phenomenon and field-induced phase transformations. ACS Appl Mater Interfaces, 2018, 10: 8818-8826
21 Chang P, Zhang Y, Du G, et al. Experiment and modeling of dynamical hysteresis in thin film ferroelectrics. Jpn J Appl Phys, 2020, 59: SGGA07
22 Tan Y, Zhang J, Wu Y, et al. Unfolding grain size effects in barium titanate ferroelectric ceramics. Sci Rep, 2015, 5: 9953
23 Mueller S, Mueller J, Singh A, et al. Incipient ferroelectricity in Al-doped HfO_2 thin films. Adv Funct Mater, 2012, 22: 2412-2417
24 Schroeder U, Yurchuk E, Muller J, et al. Impact of different dopants on the switching properties of ferroelectric hafnium oxide. Jpn J Appl Phys, 2014, 53: 08LE02
25 Fischer D and Kersch A. The effect of dopants on the dielectric constant of HfO_2 and ZrO_2 from first principles. Appl Phys Letts, 2008, 92: 012908
26 Chang P, Du G, and Liu X. Design space for stabilized negative capacitance in HfO_2 ferroelectric-dielectric stacks based on phase field simulation. Sci China Inf Sci, 2021, 64: 122402
27 Tagantsev A K, Stolichnov I, and Setter N. Non-Kolmogorov-Avrami switching kinetics in ferroelectric thin films. Phys Rev B, 2022, 66: 214109
28 Jia X, Xiang J, Xu H, et al. Depolarization Field in FeFET Considering Minor Loop Operation and Charge Trapping. IEEE Trans Electron Devices, 2022, 69: 2711-1717
29 Chang P, Du G, Kang J, et al. Conduction mechanisms of metal-ferroelectric-insulator-semiconductor tunnel junction on n- and p-type semiconductor. IEEE Electron Device Lett, 2021, 42: 118-121
30 Chang P, Du G, Kang J, et al. Guidelines for ferroelectric-semiconductor tunnel junction optimization by band structure engineering. IEEE Trans Electron Devices, 2021, 68: 3526-3531
31 Lee W C and Hu C. Modeling gate and substrate currents due to conduction- and valence-band electron and hole tunneling. In: Symposium on VLSI Technology, Honolulu, USA, 2000. 198-199
32 Shi Y, Ma T P, Prasad S, et al. Polarity dependent gate tunneling currents in dual-gate CMOSFETs. IEEE Trans Electron Devices, 1998, 45: 2355-2360
33 Grenouillet L, Francois T, Coignus J, et al. Nanosecond laser anneal (NLA) for Si-implanted HfO_2 ferroelectric memories integrated in back-end of line (BEOL). In: Symposium on VLSI Technology, Honolulu, USA, 2020
34 Gao X S, Liu J M, Au K, et al. Nanoscale ferroelectric tunnel junctions based on ultrathin $BaTiO_3$ film and Ag nanoelectrodes. Appl Phys Letts, 2012, 101: 142905
35 Park M H, Lee Y H, Kim H J, et al. Surface and grain boundary energy as the key enabler of ferroelectricity in nanoscale hafnia-zirconia: a comparison of model and experiment. Nanoscale, 2017, 9: 9973-9986
36 Mulaosmanovic H, Breyer E T, Mikolajick T, et al. Ferroelectric FETs with 20-nm-thick HfO_2 layer for large memory window and high performance. IEEE Trans Electron Devices, 2019, 66: 3828-3833
37 Ni K, Chakraborty W, Smith J, et al. Fundamental understanding and control of device-to-device variation in deeply scaled ferroelectric FETs. In: Symposium on VLSI Technology, Kyoto, Japan, 2019. 40-41